Numerical and experimental study of the effects of wind turbine operation on sand-dust transport characteristics

Gaosheng Ma[1,2,3], Hong Han[1], Ye Li[2,4*], Deshun Li[1,2,3*], Yan Wang[1,2,3], Ning Fu[1], Quan Zheng[1], and Rennian Li[1,2,3]

[1] *School of Energy and Power Engineering, Lanzhou University of Technology, Lanzhou 730050, China;*
[2] *Gansu Provincial Technology Center for Wind Turbines, Lanzhou 730050, China;*
[3] *Key Laboratory of Fluid Machinery and Systems, Lanzhou 730050, China;*
[4] *Multiple Function Towing Tank Laboratory, State Key Laboratory of Ocean Engineering, School of Naval Architecture, Ocean and Civil Engineering, Shanghai Jiao Tong University, Shanghai 200240, China*

Given factors such as reduced land availability for onshore wind farms, wind resource enrichment levels, and costs, there is a growing trend of establishing wind farms in deserts, the Gobi, and other arid regions. Therefore, the relationship between sand-dust weather environments and wind turbine operations has garnered significant attention. To investigate the impact of wind turbine wakes on sand-dust transportation, this study employs large eddy simulation to model flow fields, coupled with an actuator line model for simulating rotating blades and a multiphase particle in cell model for simulating sand particles. The research focuses on a horizontal axis wind turbine model and examines the motion and spatiotemporal distribution characteristics of four typical sizes of sand particles in the turbine wake. The findings reveal that sand particles of varying sizes exhibit a spiral settling pattern after traversing the rotating plane of wind turbine blades, influenced by blade shedding vortex and gravity. Sand particles tend to cluster in the peripheries of the vortex cores of low vorticity in the wind turbine wake. The rotation of wind turbines generates a wake vortex structure that causes a significant clustering of sand particles at the tip vortex. As the wake distance increases, the particles that cluster at the turbine's tip gradually spread outward to approximately twice the rotor diameter and then begin to mix with the incoming flow environment. Wind turbines have a noticeable impact on sand-dust transportation, hindering their movement to a significant extent. The average sand-blocking rate exhibits a trend of initially increasing and then decreasing as the wake distance increases. At its peak, the sand-blocking rate reaches an impressive 67.55%. The presence of wind turbines induces the advanced settling of sand particles, resulting in a "triangular" distribution of the deposition within the ground projection area of the wake.

wind turbine, particle transportation, actuator line model, dry deposition, particle clustering

PACS number(s): 47.55.Kf, 47.27.wb, 89.30.Ee, 92.40.Gc, 47.85.Gj

1   Introduction

As a renewable energy source with clean and widely dis-
tributed resources, wind power has garnered the attention and investment of numerous countries committed to developing low-carbon economies, leading to rapid growth in the wind power industry. However, after years of development, the site selection for onshore wind power has expanded from

*Corresponding authors (Ye Li, email: ye.li@sjtu.edu.cn; Deshun Li, email: lideshun_8510@sina.com)

relatively densely populated areas to low-cost sandy desert Gobi regions with minimal noise pollution impact or frequent sandstorms [1]. Wind is a common factor in desertification, sandstorms, and wind power generation. This means that the distribution of wind resources and areas affected by desertification are closely related. While northwest China has abundant wind resources, the Gobi Desert covers a large area. Meanwhile, even if a wind turbine is located outside of the desert region, it may still be exposed to the path of sandstorms, causing the wind turbine to operate in a dusty environment for extended periods. Strong winds are a crucial prerequisite for the occurrence of sand-dust weather. Consequently, our team is also focusing on investigating the impact of turbulent sand-laden wind fields with high Reynolds numbers on both the power output and load of wind turbines [2-5]. The present study investigates the impact of complex wake on sand-dust transport, which is of great significance for environmental issues such as air quality around and downstream of wind farms. It also contributes to the analysis of dust dry deposition in the wake-affected area inside wind farms, thus analyzing the development of surface ecology (desertification). The results can provide technical support for advancing environmentally friendly wind energy.

At present, there is a dearth of research on the impact of wind turbine operation on sand-dust transport characteristics. Most scholars focus on the effects of wind farms on rainfall and temperature distribution [6,7], but some scholars have also carried out studies on the dispersion and deposition of pollutants within wind farms. For instance, Mo et al. [8] utilized numerical simulation methods to investigate the spatiotemporal distribution of pollutants surrounding wind farms, revealing an "edge effect" where pollutants cluster in the upwind and adjacent boundary regions. Wang et al. [9] utilized weather research and forecasting (WRF) model to assess the effects of wind farms on the atmosphere environment and discovered that their presence facilitated the redistribution of atmospheric pollutants, leading to regional diffusion and transport. More compelling is the evidence from observational data. In 2018, Wang et al. [10] quantified the level of microplastic pollution in offshore wind farms located in the Yellow Sea of China and discovered that wind farms can increase the bed shear stress during ebb tide, disturbing the bed sediment, and facilitate detachment of microplastics attached to sediment. All the aforementioned studies have yielded favorable outcomes, however, they are for the wind farm scale, and there is a dearth of analysis about the dynamic behavior of sand particles on the wake scale of wind turbines. Specifically, the spatiotemporal distribution characteristics of dust within the influence range of an individual wind turbine remain unclear.

In this way, the research will delve into the two-phase flow problem of particle-turbulence interaction. Numerous studies have demonstrated that distinct Stokes numbers and volume fractions determine the unidirectional or bidirectional coupling between particles and turbulence, with particles even capable of suppressing or enhancing turbulence [11-13]. Conversely, the collective dynamic behavior of a large number of particles is also highly intriguing.

In the study of sand particle distribution in boundary layer shear flow, Gunn et al. [14] conducted field observation experiments to demonstrate that sand-dust transport comes from nonequilibrium atmospheric boundary layer convection by measuring atmospheric wind, humidity, and temperature profiles, along with measurements of sediment transport. According to the reported findings, an unstable atmospheric boundary layer also has a significant impact on sand-dust transport, and the particle size distribution of dust is not only associated with friction velocity but also atmospheric stability [15]. He et al. [16] employed large eddy simulation coupled with the Lagrange particle tracking method to establish a sandstorm movement model that takes into account unstable atmospheric boundary layer. They discovered that when wind speed is close to the particle starting threshold, an unstable atmospheric boundary layer has a significant impact on the sand-dust transport rate. However, as wind speed increases, this effect gradually weakens. In the investigation of two-phase particle-air flow passing through obstructions, Luo et al. [17] employed direct numerical simulation to examine three-dimensional motion around a cylinder and discovered that particles with varying Stokes numbers exhibit distinct dispersion characteristics, leading to diverse modes of interaction between particle and cylinders. Yao et al. [18] observed the particle concentration distribution in the two-dimensional passing flow through a disk and discovered that the particles were concentrated between periodic shadow vortices. Homann et al. [19] performed direct numerical simulations of inertial particles in the wake of a sphere and found them to form preferential concentrations both in the sphere boundary layer and in its wake. Due to the effect of the shedding vortex, the particle concentration in a region downstream of the sphere exceeds the concentration in the incoming flow. Shi et al. [20,21] employed one-way coupled three-dimensional numerical simulations to investigate the inhomogeneous distribution of inertial particles in the unsteady flow around a wetted circular cylinder. The bow shock-like clustering was explored via Voronoi diagrams and discovered that the width and thickness of the bow shock strongly depend on the Stokes number. Lin et al. [22] numerically simulated a three-way coupled flow of particle-laden fluid around a square obstacle using a finite-volume and discrete-element coupling method to explore the dynamics of each phase and the modulation mechanism of the flow field by inertial particles. While all of the above studies dealt with particle-laden flow under stationary obstacles, the anchoring scenario in this study is a high Reynolds number particle-laden flow under the combined effect of wind tur-

bine blade rotation, nacelle and hub wake, and atmospheric boundary layer shear, which produces a more complex wake than the above study.

Nonetheless, there are still scholars who have carried out similar studies. Smith et al. [23] conducted a wind tunnel experiment utilizing PIV to investigate the behavior of droplets in wind turbine wake and their impact on wake recovery. The study revealed that droplets exhibit clustering behavior at various locations within the wake, which affects the turbulence statistics. Immediately following this, Travis et al. [24] conducted a wind tunnel experiment to investigate the coupling relationship between inertial particles (droplets) and turbulent wake in porous disk generators. Their findings revealed a distinct difference in the wake structure when inertial particles were present in the flow. Moreover, distinct structures are present in the near and far wake zones, which exhibit variations based on the particle volume fraction. These findings collectively demonstrate that particles with different Stokes numbers exhibit diverse transport characteristics in turbulent flow; however, the dynamic behavior of constant-size particles cannot be investigated through wind tunnel experiments.

Therefore, this study employs large eddy simulation to model flow fields, coupled with the actuator line model for simulating rotating blades and the multiphase particle in cell model for handling sand particles. The aim is to reveal the motion patterns of typical sizes of sand particles in the wake of the wind turbine under varying levels of dust weather environments, as well as the spatiotemporal distribution characteristics of the sand particle concentrations within the influence area of an individual wind turbine. This study will establish a theoretical foundation for subsequent engineering challenges, such as nacelle sealing and tower and blade wear, faced by industry professionals.

2   Methodology

The wind-sand flow problem investigated in this paper employs the Eulerian formalism to describe fluid flow and the Lagrangian formalism to describe solid particles. The motion of solid particles is evaluated using a multiphase particle in cell model in particle flow modeling, while an actuator line model is used to simulate the rotating blades of wind turbines. A key challenge in the modeling process lies in coupling these two methods.

2.1   Multiphase particle in cell

The multiphase particle in cell (MP-PIC) method is a coarse-grained approach used to solve gas-solid two-phase systems, initially introduced by Andrews et al. [25]. As a hybrid Euler-Lagrange method, it employs volume-averaged Na-

vier-Stokes equations to describe the fluid phase in the gas, while discretizing the particle phase using numerical particles. The method considers a group of real particles as a parcel, tracking each parcel to obtain the spatial distribution of the particle phase at different time points. This approach greatly enhances computational speed without compromising result accuracy under most conditions. Unlike traditional discrete phase methods (DPM), the MP-PIC method utilizes solid phase stress to represent inter-particle forces, further improving computational efficiency.

In the MP-PIC method, the continuity and momentum equations for gas-phase flow based on volume averaging are

$$\frac{\partial(\varepsilon_g \rho_g)}{\partial t} + \nabla \cdot (\varepsilon_g \rho_g u_g) = 0, \tag{1}$$

$$\frac{\partial(\varepsilon_g \rho_g u_g)}{\partial t} + \nabla \cdot (\varepsilon_g \rho_g u_g u_g)$$
$$= -\varepsilon_g \nabla p + \nabla \cdot \varepsilon_g \tau_g + \varepsilon_g \rho_g g - F, \tag{2}$$

where, ε_g is the gas-phase volume fraction, ρ_g is the gas-phase density, u_g is the gas-phase velocity, τ_g is the gas-phase stress tensor, F is the drag force on particles, and g is the gravitational acceleration.

In the MP-PIC method, the solid phase uses the discrete particle method, which takes into account the drag force of the particles, the gravitational force, and the contact force of the particles colliding with each other. Since the volume fraction of particles in sandstorm weather is less than 10^{-6}, it is a dilute phase flow [26]. Therefore, the contact force of particles colliding with each other is ignored in the calculations, and only the drag force and gravity of particles are considered. In contrast to the gas-phase equation, the distribution of solid-phase particles in space is described by the particle distribution function $f(x, u_p, \rho_p, V_p, t)$. This function represents the probability of finding a particle with velocity u_p, density ρ_p, and volume V_p at position x_p and time t. The evolution of f with time t is denoted as:

$$\frac{\partial f}{\partial t} + \nabla \cdot (u_p f) + \nabla u_p \cdot (A_p f) = 0, \tag{3}$$

where f is the particle distribution function, A_p is the particle acceleration.

At every instant, the position and velocity of each parcel are determined by applying Newtonian equations of motion:

$$\frac{dx_p}{dt} = u_p, \tag{4}$$

$$\frac{du_p}{dt} = -\frac{\nabla p}{\rho_p} - \frac{\nabla \tau_p}{\varepsilon_p \rho_p} + g + \frac{\beta_p}{\rho_p}\left(u_g(x_p) - u_p\right), \tag{5}$$

where β_p is the drag force coefficient, ε_p is the solid phase volume fraction, and ρ_p is the average solid phase density. The relationship between the solid phase volume fraction ε_p and the gas phase volume fraction ε_g at any point in the flow field is satisfied:

$$\varepsilon_p + \varepsilon_g = 1. \tag{6}$$

The expression for the solid phase stress τ_p is given as:

$$\tau_p = \frac{p_s^* \varepsilon_p^\alpha}{\max\left[\varepsilon_{\text{pmax}} - \varepsilon_p, \zeta(1 - \varepsilon_p)\right]}, \tag{7}$$

where p_s^* and α are both model coefficients, which typically take the values of $10 \leqslant p_s^* \leqslant 100$ and $2 \leqslant \alpha \leqslant 5$, $\varepsilon_{\text{pmax}}$ is the maximum value of the particle volume fraction, and ζ is an artificially set decimal of magnitude 10^{-7} to avoid a denominator of zero.

The gas phase is coupled to the solid phase by a drag force F. The relationship between F and the particle distribution function f is given as:

$$F = \iiint f V_p \left[\beta_p(u_g - u_p) - \nabla p\right] \mathrm{d}V_p \mathrm{d}\rho_p \mathrm{d}u_p. \tag{8}$$

Due to the wide range of particle concentration variations involved, the Ergun-WenYu drag model, which incorporates a wide range of particle concentrations, was used in the simulations.

2.2 Actuator line model

The actuator line model (ALM), initially proposed by Sørensen and Shen [27], simplifies a wind turbine blade to a virtual line that bears a body force. This line is divided into a finite number of actuator elements, each of which is subjected to a force acting on its midpoint (actuator point). In the calculation process, the wind speed and attack angle on each actuator point are first obtained, and then the lift and drag force exerted on each actuator point is determined by looking up existing airfoil data. The ALM simulates the action of the blade on the flow field by loading the body force on the actuator point and solves the Navier-Stokes equations to obtain the wake field characteristics. This approach eliminates the need for modeling an entity wind turbine structure and considering the blade surface boundary layer. Therefore, it is suitable for simple structured grids and reduces the computation time. The ALM accurately characterizes the reaction force of blades on the incoming flow and is commonly combined with the Large Eddy Simulation (LES) method. In this study, the Smagorinsky subgrid model is employed for LES.

The body force at each actuator point in the ALM can be expressed as:

$$f_{2D} = (L, D) = \frac{1}{2}\rho U_{\text{rel}}^2 c(C_L e_L, C_D e_D), \tag{9}$$

where, U_{rel} is the resultant velocity of the incoming flow at the airfoil section, c is the chord length of the airfoil, ρ is the density of the flow field, C_L and C_D are the lift and drag coefficients of the airfoil, e_L and e_D are unit vectors in the direction of lift and drag.

To prevent singularities in the numerical calculations, the body force at each point on the actuator line is distributed in a three-dimensional Gaussian form within a sphere centered at that point. The body force at any point in the flow field can be expressed as:

$$f_\varepsilon(s, d) = \int_0^R f_{2D} \cdot \eta_\varepsilon(d) \cdot \mathrm{d}s, \tag{10}$$

where d is the distance from the center of the grid to the actuator point, s is the distance from the actuator point to the center of the hub, R is the rotor radius, and $\eta_\varepsilon(d)$ is the body force distribution function.

$$\eta_\varepsilon(d) = \frac{1}{\varepsilon^3 \pi^{3/2}} \exp\left[-\left(\frac{d}{\varepsilon}\right)^2\right], \tag{11}$$

where ε is the Gaussian distribution factor, which controls the density of the body force distribution.

The transport process of sand particles is primarily influenced by atmospheric turbulence. In actuality, the presence of a wind turbine leads to a minimal number of particles colliding with the turbine blades and altering their trajectory. Rather, it is the wake generated by the wind turbine's operation that serves as the main propelling force behind sand-dust transportation. Various studies have demonstrated that ALM effectively reproduces the wake field of wind turbine blades [28-30], a characteristic that aligns with the focus of this paper.

To conduct numerical simulation studies on wind-sand two-phase flow in wind turbines, this paper proposes a solver called ALM and MPPICFoam based on OpenFOAM, which combines the MP-PIC method and ALM. The existing MPPICFoam solver of OpenFOAM is coupled with ALM by adding a source term of the body force to the momentum equation. In the solution, the force and coordinate information of the particles are first calculated based on the particle boundary conditions, and then the body force is calculated based on the parameters of the wind turbine. In the fluid phase solution, the reaction force of the particles on the flow field and the body force obtained from the actuator line are loaded onto the flow field to participate in the solution of the Navier-Stokes equations. In the particle phase solution, the particle forces are calculated based on the information of the flow field, and their velocities and positions are updated by the integral Newtonian equations of motion.

Taking the MP-PIC control equation as a basis and adding the body force G of ALM to its momentum equation (eq. (2)), the fluid-phase flow is described by the volume-averaged-based momentum equation as:

$$\frac{\partial(\varepsilon_g \rho_g u_g)}{\partial t} + \nabla \cdot (\varepsilon_g \rho_g u_g u_g)$$
$$= -\varepsilon_g \nabla p + \nabla \cdot \varepsilon_g \tau_g + \varepsilon_g \rho_g g - F + G. \tag{12}$$

2.3 Computational setup

The physical model depicted in Figure 1 illustrates the flow of a fluid containing finite-sized particles around a rotating wind turbine, with randomly distributed particles entering the domain at the same velocity as the fluid.

The wind turbine model utilized in this study is a three-bladed design developed by the Gansu Provincial Technology Centre for Wind Turbines, featuring a rotor diameter of D=0.44 m and hub center height of H_{hub}=0.65 m, with SG6050 airfoil blades. TSR=6.4 ($TSR = \omega R / U_\infty$ is the tip speed ratio of wind turbine defined as the ratio between the wind turbine blade tip linear velocity and the wind speed). The wind turbine is positioned along the flow direction at the centerline of the computational domain, with distances of $5D$ and $20D$ from the inlet and outlet respectively. The computational domain measures 11 m×1.4 m×1.35 m, equivalent to approximately $25D \times 3D \times 3D$. As per previous research [31], the typical size of a computational domain ranges from ($7D$-$15D$) × ($2D$-$5D$) × ($2D$-$5D$). Therefore, the current setup of the computational domain satisfies all requirements. The boundary condition for the incoming flow is a steady uniform incoming flow of 6.6 m/s, and the outlet boundary is a zero-gradient condition. The top, bottom, front, and back surfaces are all subjected to wall boundary conditions. The pressure boundary conditions were all set to zero gradient. The particles are uniformly injected from the inlet surface at 168000 particles per second at the same velocity as the surrounding fluid. Particle stick boundary conditions are applied to the bottom surfaces, while other surfaces allow particles to escape.

The mesh partitioning process utilizes the blockMesh and snappyHexMesh tools provided by OpenFOAM. The initial background mesh is divided into three directions: flow direction, lateral direction, and vertical direction, with 220 nodes in the flow direction, 28 nodes in the lateral direction, and 27 nodes in the vertical direction. Meanwhile, to meet the requirements of the actuator line body force and enhance the capturing capability of the wind turbine wake, a three-layer encryption scheme is applied to the computational domain mesh, as illustrated in Figure 2. Specifically, box1 is used to encrypt the wind turbine rotating region and wind turbine wake zone. Additionally, box2 and box3 are employed for grid transition to minimize the impact of different grid sizes at the encrypted boundaries in the flow direction on computational results. The minimum mesh size is 0.00625 m and the total number of mesh is about 6 million.

According to observations [32,33], the surface particle size distribution during sandstorms approximates a lognormal distribution, with the highest probability of sand particles between 90-100 μm in size. Moreover, as height increases, the expected value of the particle size gradually decreases. During the floating dust period, the dust mass concentration
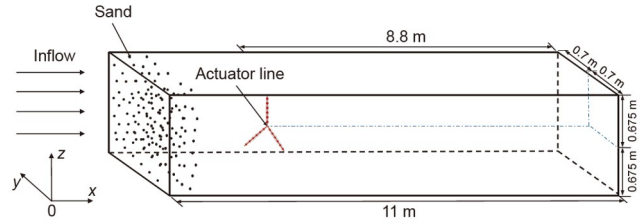

Figure 1 (Color online) A schematic of the particle-laden flow configuration.

Figure 2 (Color online) Computational domain and meshing.

was less than 31.62 μg m^{-3}. During the blowing sand stage, the sand mass concentration was less than 316.23 μg m^{-3}. During sandstorms, the sand mass concentration ranged from 1220 to 42146 μg m^{-3}, with an average mass concentration of 9287 μg m^{-3}. During sand and dust transport, particles of various sizes will show different distributions in the height space. Especially at the height at which the wind turbine blades operate, the main particle size of sand particles is concentrated in the range of 10-110 μm [34]. Even larger-sized particles can occur at certain specific sand sources. Therefore, taking into account the different dust weather levels and the characteristics of the sand source.

In this paper, four typical particle sizes with d_p=10, 50, 100 and 150 μm were considered corresponding to St=0.01, 0.30, 1.23, 2.78 ($St = \tau_s / \tau_f$ is the Stokes number defined as the ratio between the particle relaxation time $\tau_s = \rho_p d_p^2 / 18\mu$ and the characteristic time scale of fluid $\tau_f = \theta / U_\infty$), which were both smaller than the grid size. Specific parameters outlined in Table 1.

3 Numerical model validation

To evaluate the reliability of the ALM and MPPICFoam solver, we compared the simulation results of this study with data from our team's previous wind tunnel experiments [35]. The experiments were conducted in the environmental wind tunnel of the Key Laboratory of Western Disaster and Environment of the Ministry of Education, Lanzhou University. Figure 3(a) illustrates the wind tunnel, which has a total length of 40 m and comprises an inlet rectification section, a test section, an outlet section, and a fan system. The test section measures 20 m in length with a cross-section dimension of 1.4 m×1.3 m, capable of reaching maximum wind speeds of up to 30 m/s. The wind tunnel is equipped with a sand release device, located 2 m from the entrance of

Table 1   Detailed parameters of each numerical case, where Case A is the control group, no sand

Case	U_∞ (m/s)	TSR	d_p (μm)	ρ_p (kg/m³)	St	N_p	C (μg/m³)
A	6	5.5	–	–	–	–	–
B	6.6	6.4	10	2650	0.01	168000	18
C	6.6	6.4	50	2650	0.30	168000	2335
D	6.6	6.4	100	2650	1.23	168000	18687
E	6.6	6.4	150	2650	2.78	168000	63069
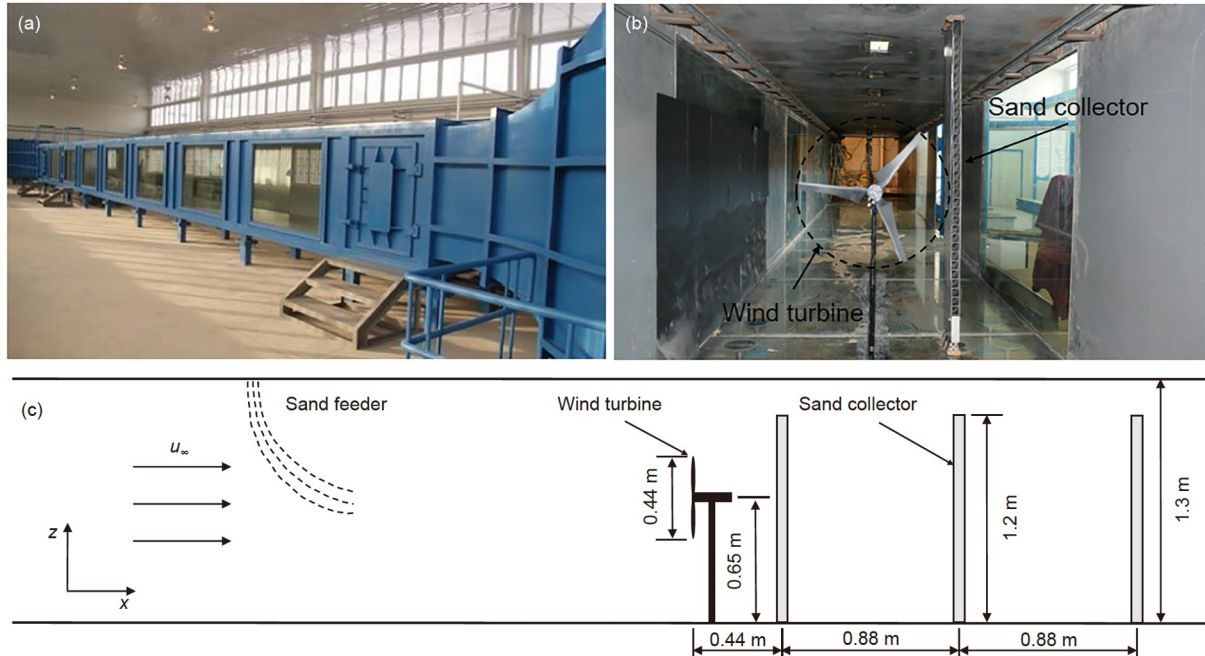
Figure 3   (Color online) (a) The diagram of a wind tunnel; (b) schematic diagram of wind turbine model and sand collector; (c) schematic diagram of the experimental setup.

the test section. This device, perpendicular to the flow direction, consists of a 0.3-meter-long structure with an adjustable sand slit at its bottom. The sand particles are released freely due to gravity. Sand collectors were strategically placed behind the wind turbine at various distances to measure sand particle concentration distribution (Figure 3(b)).

Figure 4(a) shows a comparison between the simulated and experimental results for the axially averaged velocity of the wind turbine wake. The axial velocity agrees well with the experimental data at the tip of the blade, but there is a large deviation at the hub. The main reason for this discrepancy is that the numerical calculations ignore the effect of the wind turbine hub, resulting in high wind speeds at the hub. The average error between the simulated and experimental data at the blade tip was 4.5%, indicating that the simulated data accurately modeled the actual situation at that location. The temporal evolution of the mean fluid fluctuation velocity was plotted at x=0.44 m, y=0 m, and z=0.5 m in Case A (Figure 4(b)). The mean fluid fluctuation velocity reached a steady state after t=1.5 s. Therefore, all data obtained from the

calculations were based on average values during the 1 s period following the initial state of 4 s to reach stability.

The conclusions drawn from the experiment (Figure 5) indicate that during wind turbine rotation, sand particles experience a combined effect of obstruction caused by the turbine, collisions with the blades, and tip vortex, resulting in a noticeable clustering phenomenon [36]. The region of clustering aligns closely with the position of the tip vortex. Additionally, circular bands are observed in the cross-section, which closely resembles our simulation results. The accuracy of the simulation can be further demonstrated, thereby indicating the feasibility of employing numerical methods to investigate the impact of wind turbine operation on sand-dust transport characteristics.

4   Results and discussion

To examine the motion characteristics of sand particles within the wake of a wind turbine and assess the impact of
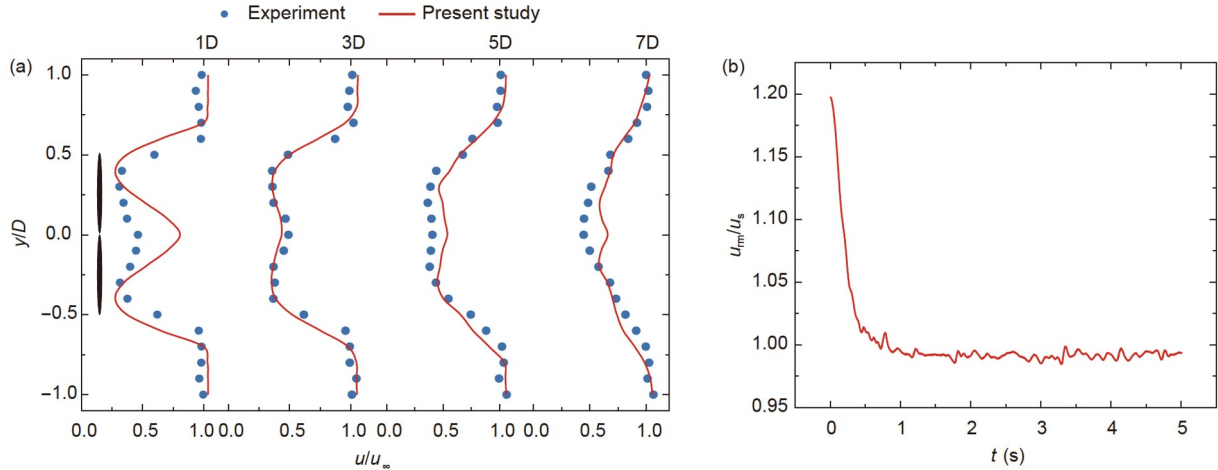
Figure 4 (Color online) (a) Case A: axial velocity profile of the wake stream; (b) temporal evolution, Case A: x=0.44 m, y=0 m, z=0.5 m.
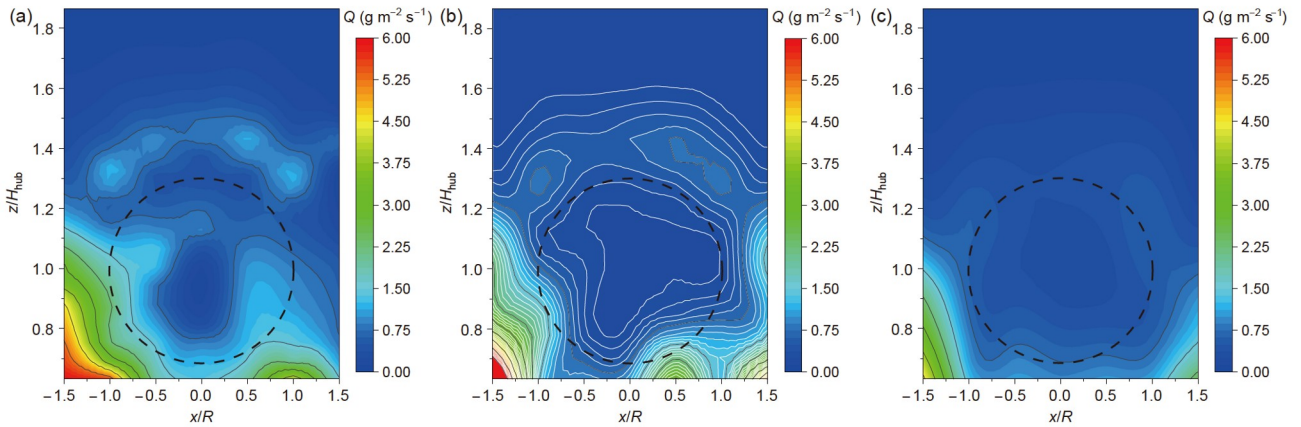

Figure 5 (Color online) Sand transport flux distribution. (a) x/D=1; (b) x/D=3; (c) x/D=5.

said wake on the spatial distribution of sand particles, the hexahedral region with a thickness of 0.02 m at 0.2D, 0.5D, 0.7D, 1D, 2D, 3D, 5D, 7D, and 9D cross-section locations behind the wind turbine is regarded as a cross-section as shown in Figure 6.

4.1 Analysis of the motion behavior of sand particles in wind turbine wake

The wake of a wind turbine is a three-dimensional complex turbulence resulting from the interaction between the atmospheric boundary layer and rotating blades, which causes a reduction in axial airflow velocity and rotation in the near wake zone [37,38]. During the formation of sandstorms, turbulence in the near-surface shear layer causes sand particles to be lifted off the surface and suspended in the air, especially when passing through the sand source. The lifting of sand particles depends on several factors, including wind speed, wind direction, and surface roughness. Overall, sand

particle lifting is a complex physical process that is the combined result of the interaction of multiple factors. The focus of our study is on the effect of wind turbine operation on sand-dust transport, not on the mechanism of sand particle lifting or the process of sandstorm development. Therefore, sand lifting is not considered in our computational model for the time being. Such considerations do not materially affect the results of our study of wind turbine transport of sand-dust particles. An aerial view of the spatial location distribution of sand particles and the wind turbine wake vorticity is shown in Figure 7, which shows that the sand particles enter the wind turbine wake zone and interact significantly with the wake.

Figure 8 illustrates the average velocity distribution of sand particles at different cross-sections along the axial position. A high-velocity region in the axial velocity at the center of the hub is observed at the x/D=1 cross-section, which is caused by the fact that the ALM does not take the hub into account. Furthermore, the figure illustrates that the
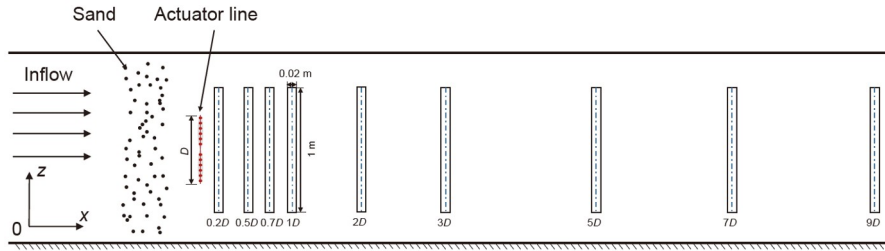
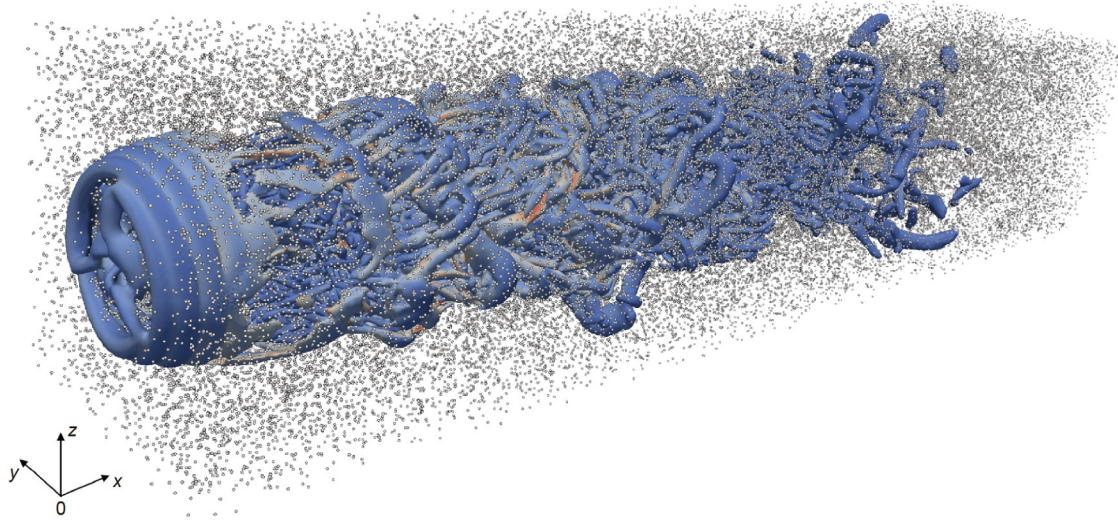**Figure 6**   (Color online) Schematic diagram of the data collection area.

Figure 7   (Color online) Case C: Aerial view of sand particles location and wind turbine wake vortices.
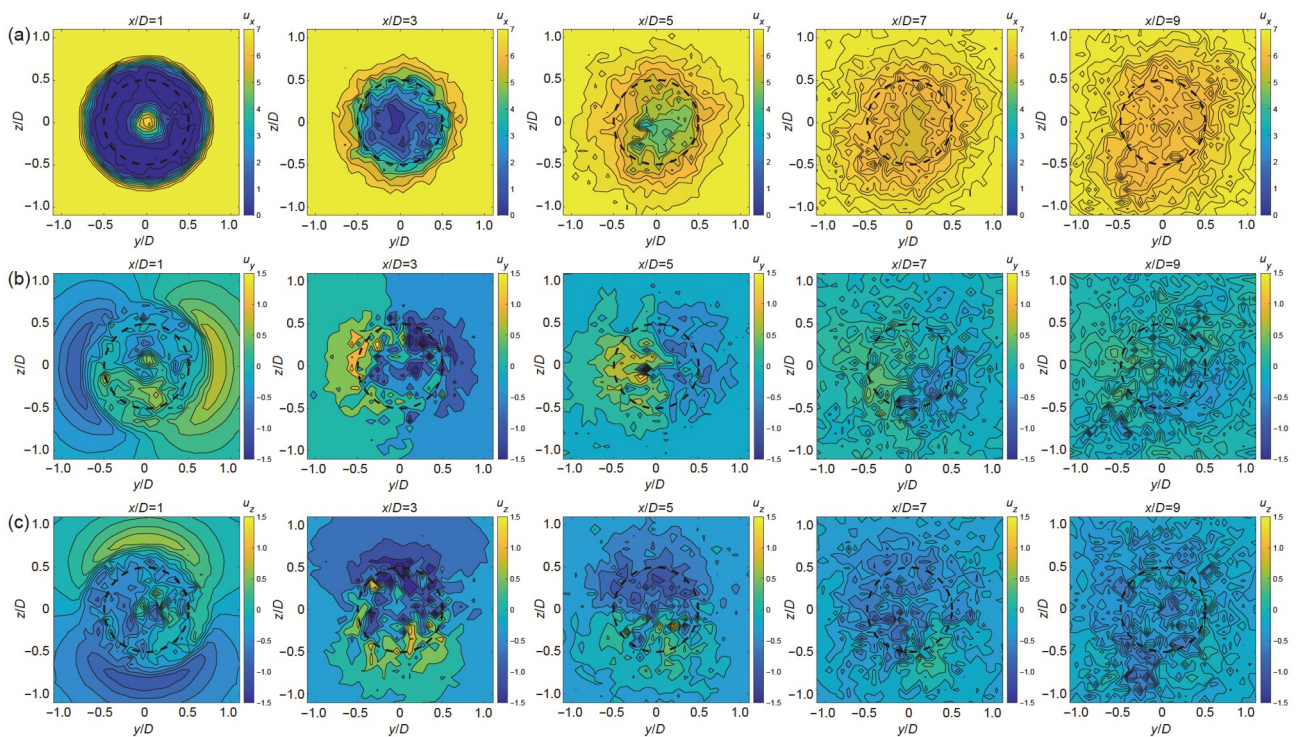

Figure 8   (Color online) Case C: Average velocity cloud map of sand particles, x/D=1, 3, 5, 7, 9. (a) u_x, (b) u_y, (c) u_z.

axial velocities of particles within the rotational range of the wind turbine are significantly lower than those outside. The reason for this is that, based on the wind turbine vortex theory, as the airflow passes through the wind turbine blades, the rotational angular momentum of the wind is extracted by the wind turbine, while at the same time, the airflow itself gains an opposite angular momentum. Consequently, particle axial velocity decreases accordingly as the airflow passes through, while the tangential velocity increases correspondingly.

The mean velocity distributions in the lateral and vertical directions indicate that particles undergo rotation and outward expansion within the near wake zone, as demonstrated more clearly in the particle velocity vector diagram in Figure 9. With the increase in axial distance of the wake, the wake gradually recovers after interacting with turbulence from the surrounding atmosphere. As a result, there is a decrease in lateral velocity and a weakening of particle rotation effects. Analysis of average particle velocity field statistics on various lateral and vertical planes reveals that particles exhibit pronounced rotational characteristics within the near wake zone, while such rotation effects diminish within the far wake zone, leading to stable particle velocities. This phenomenon bears a striking resemblance to the evolution of wind turbine wakes over distance.

As the wind turbine blades rotate, a complex vortex structure is formed to perturb the flow field. Over time, large-scale structures gradually pass to smaller-scale structures. In turbulent flows, small-scale structures typically have higher dissipation rates, indicating that energy is dissipated more quickly. The high rotational speed of the modeled wind turbine used in this study results in a relatively fast recovery of the wake velocity, which can cause rapid dissipation of the vortex [39]. On the other hand, the rapid dissipation of the vortex may also be due to the inability of the grid resolution in the far wake zone to capture the small-scale structures in the flow field. The motion of sand particles in the wind turbine wake is closely related to the vortex structure in the wake. As shown in Figure 10, the distribution of particles in the instantaneous vortex cloud maps of the wind turbine wake under different cases of sand particle size changes accordingly. 10 μm-sized particles, whose Stokes number is much smaller than 1, have less inertia and can respond to the fluid motion quickly, showing the characteristic of diffuse distribution in the vortex structure. As shown in Figure 10(a), the particles occupy almost the entire wake field and are uniformly distributed, and the contours of the vortex clusters in the wind turbine wake are poorly discerned. As the particle size increases, their inertia also increases. Under the action of centrifugal force, the particles are thrown out by the vortex structure and cannot enter the core area of the vortex clusters. The contours of the vortex cluster are progressively exposed, forming a "network
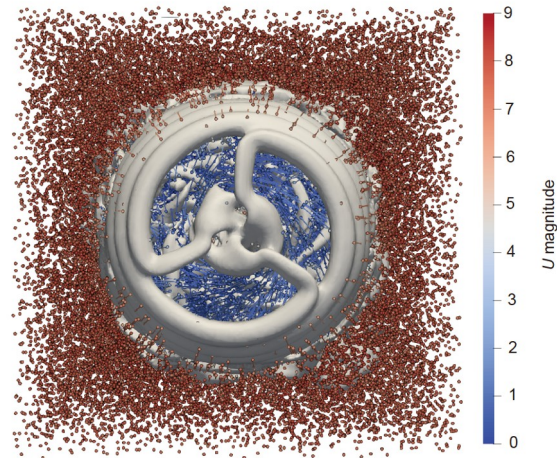

Figure 9   (Color online) Case C: 3D vector diagram of sand particles, vector direction indicates the direction of particle and velocity, and vector color indicates the particle velocity magnitude.

structure" as shown in Figure 10(b). Along with the increase of the wind turbine wake distance, the turbulence in the wake is attenuated, and the "network structure" disappears accordingly. For 100 μm-sized particles, whose Stokes number is close to 1, they are thrown out by the centrifugal action of the vortex core with high vorticity in the wake and gather at the peripheries of the vortex structures with low vorticity, and the contours of the vortex clusters become more visible, as shown in Figure 10(c). For 150 μm-sized particles, its Stokes number is greater than 1, inertia is large, and the particle relaxation time is greater than the characteristic time scale of the fluid. So it is less affected by the surrounding fluid movement, can maintain its motion characteristics, is not easy to be sucked in by the vortex, and under the action of gravity occurs an obvious settlement, as shown in Figure 10(d).

The study of the dynamic behavior of sand particles in the near wake zone of a wind turbine is of great engineering significance for the prevention and control of problems such as heat dissipation in the nacelle, bearing wear, and the failure of the wind speed anemometer on the top of the nacelle. To analyze the motion characteristics of sand particles in the near wake zone more deeply, the dashed line range of Figure 10 is locally enlarged, as shown in Figure 11. The dispersive dynamic behaviors of sand particles with four different Stokes numbers in the near wake zone exhibit distinct variations. Among these, in Case B, the distribution of sand particles does not significantly differ from the unaffected environment (non-turbine-affected area). However, their motion direction appears to be more erratic or chaotic. Combined with Figure 9, it can be judged that this is caused by the combined effect of various vortexes received in the near wake flow, and even some particles appear to move in the reverse direction along the axial direction. However, as
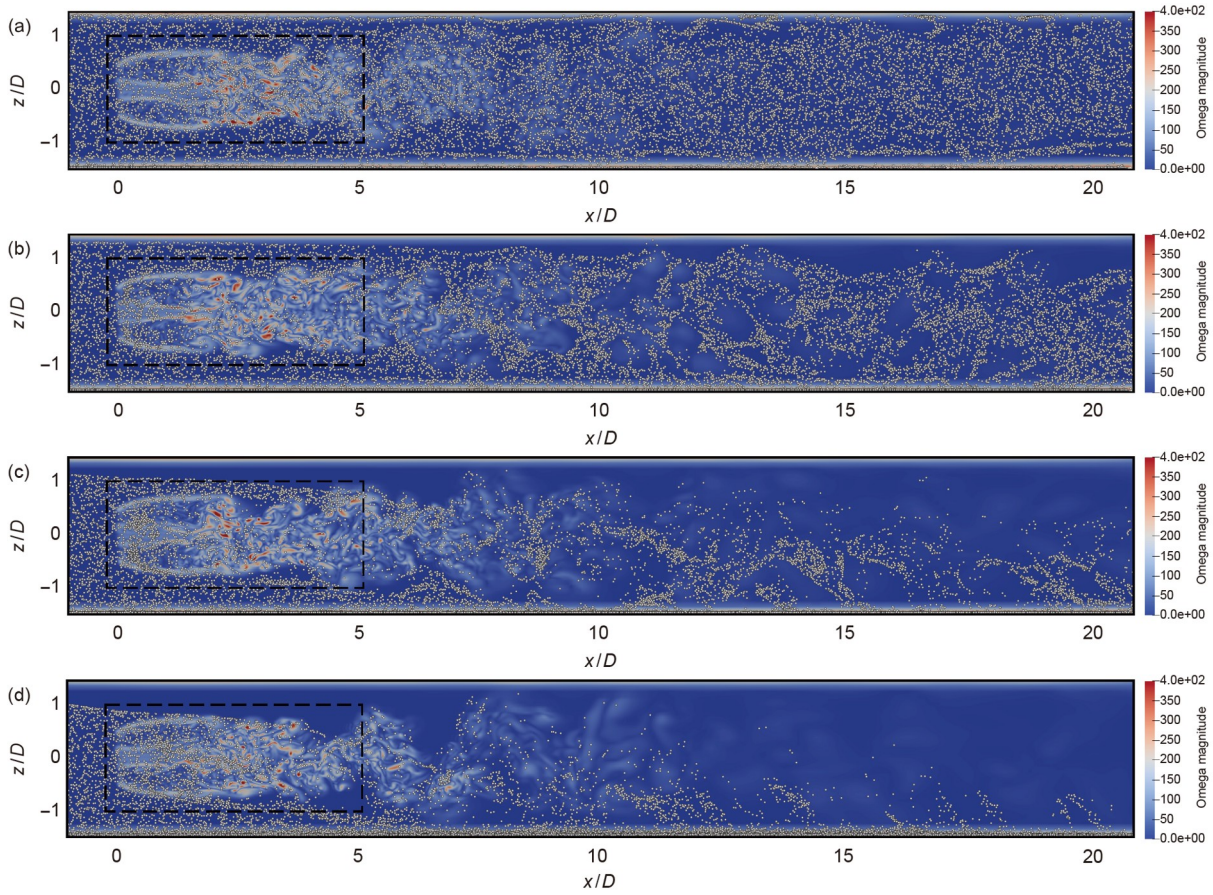
Figure 10   (Color online) Particle distributions in transient vortex cloud maps of wind turbine wake. (a) Case B; (b) Case C; (c) Case D; (d) Case E.
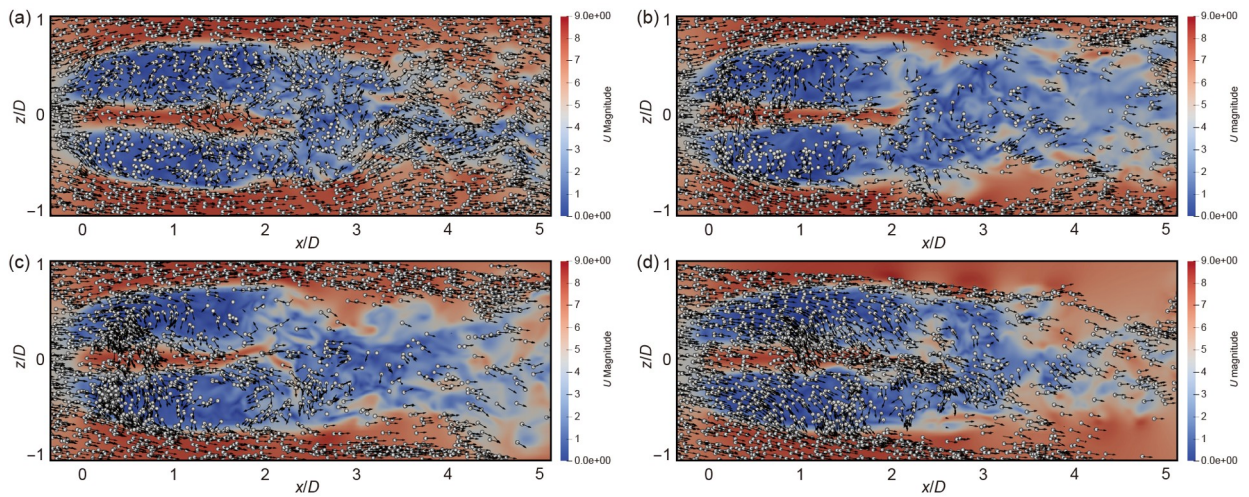

Figure 11   (Color online) Enlarged view of the instantaneous velocity field and particle distribution, with the vector direction indicating the in-plane particle velocity direction and the vector length not indicating the particle velocity magnitude. (a) Case B; (b) Case C; (c) Case D; (d) Case E.

the Stokes number increases, the percentage of particles moving in the reverse direction gradually decreases.

In addition, as the Stokes number increases, there is a significant increase in the concentration of sand particles behind the wind turbine plane in Case C, Case D, and Case E,

followed by a gradual decrease. This phenomenon can be attributed to the tendency of sand particles within this Stokes number range to cluster in regions with high vorticity, resulting in their entrapment without replenishment from behind. It could also be due to the reduction of vorticity, which

forms void regions within the sand. However, as the Stokes number increases, this phenomenon is significantly weakened. In Case E, the dust concentration becomes more uniformly distributed, resulting in a more pronounced settling phenomenon. Additionally, the number of settling particles in the near wake zone is significantly higher under the influence of gravity compared to other cases. It is worth noting that the ALM, in contrast to a physical wind turbine, does not take into account the hub. This omission results in an increased velocity at the center of the hub, causing certain particles to flow downstream along the hub center for a certain distance before merging with the surrounding particles. As a result, there exists a slight deviation from the actual situation.

4.2   Analysis of the spatial distribution of sand particles in wind turbine wake

To investigate the impact of wind turbine wake on dust concentration distribution across different altitude planes, Case C was selected to generate three horizontal cross-sectional cloud maps depicting the number of sand particles (Figure 12). The top-to-bottom sequence of images corresponded to the upper blade tip, hub center, and lower blade tip respectively. The distribution of the sand particles is approximately symmetrical. The sand particles diffuse outward to varying degrees after passing through the wind turbine, and the occurrence of clustering at the tip vortex where particle concentration increases. However, the clustering phenomenon at the upper tip height is not as significant as at the lower tip height, which is probably due to the influence of the obstruction effect caused by the closer proximity to the ground. As the distance along the axial direction increases, mixing occurs after a certain distance and the clustering phenomenon decreases. However, in terms of consistency,

the overall concentration at the lower blade tip is higher and the degree of inhomogeneity is more pronounced. It is obvious that the influence range is largest at the hub center height and furthest away at the lower blade tip height.

To further observe the distribution pattern of sand particles with different particle sizes at different heights, the number distribution of sand particles with varying sizes in the vertical cross-section was analyzed in this study, as shown in Figure 13. Since this paper simulates the wind tunnel scale, the airflow passing through the wind turbine is affected by the wall boundary conditions, which leads to an increase in the velocity and a decrease in the pressure at the tip of the wind turbine blades, resulting in the "narrow tube effect". Sand particles are accelerated by the "narrow tube effect". Considering the gravity of the particles themselves, the sand particles clustered at the upper blade tip extended a longer distance than at the lower blade tip under different Cases. In addition, the clustering and mixing of sand particles of different particle sizes varies along the axial direction. Since this simulation focuses on the intake of inlet sand, the particles are not replenished by the upper sand particles after settling, resulting in a significant sand-free zone in Case D and Case E. However, this phenomenon can also occur in cases with larger particles and insufficient sand source areas ahead. Overall, this does not affect the qualitative analysis of the effect of wind turbine wake flow on sand-dust transport.

To identify clusters from the data more efficiently, we performed a Voronoi analysis [40] on the vertical cross-section of the instantaneous particle field in Case C to observe the clustering behavior (Figure 14). Based on the perpendicular bisect method, Voronoi cells are built through the obtained center points to create the polygonal regions shown, with shape and areas defined by lines of proximity to the nearest surrounding neighbors. Large cells represent voids and small cells are particle clustering regions. Figure
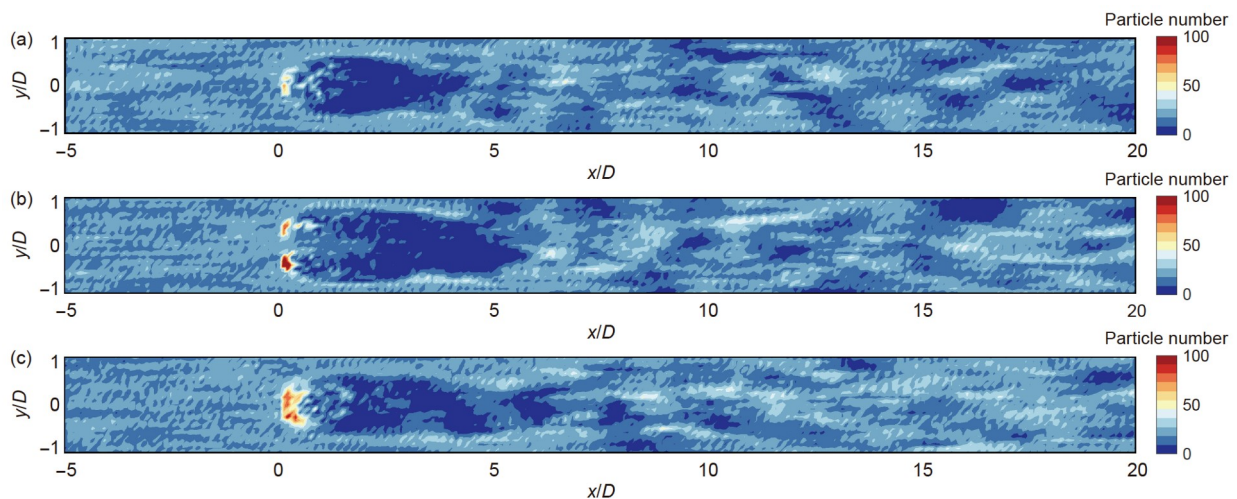

Figure 12   (Color online) Case C: Cloud maps of the number of sand particles in the horizontal cross-section of the wind turbine during operation. (a) Upper blade tip; (b) hub center; (c) lower blade tip.
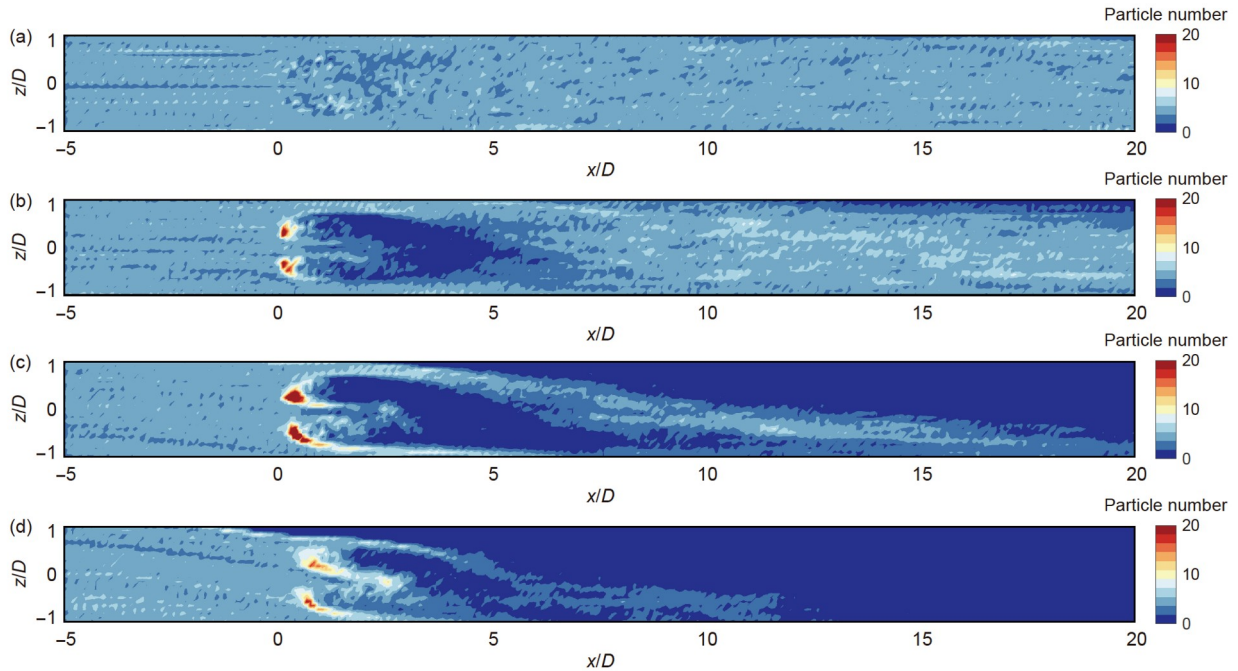
Figure 13 (Color online) Cloud maps of the number of sand particles in the vertical cross-section of the wind turbine during operation. (a) Case B; (b) Case C; (c) Case D; (d) Case E.
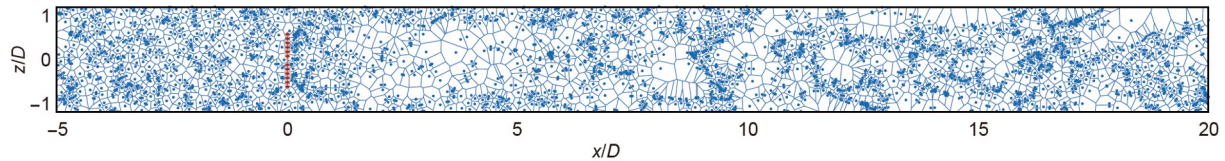

Figure 14 (Color online) Case C: Voronoi diagram of the vertical cross-section of instantaneous particle field.

14 shows that there is a clear difference in the clustering behavior of particles before and after the wind turbine. Even if the incoming flow is uniformly laminar, small-scale clustering behavior occurs due to the self-organization of the particles. Meanwhile, large gaps appear within the near wake zone of the wind turbine, which suggests that the sand particles are clustered to the peripheries of the wake zone. In the far wake zone, clusters of different length scales appear, indicating that as the wake distance increases, the tip vortices decay and mix with the flow vortices in the flow field to form a large-scale structure, which also explains the "network structure" observed in Figure 10.

The detailed analysis in Figure 15 illustrates the distribution of sand concentration at various locations surrounding the wind turbine. The spatial distribution of sand particles under different particle size cases exhibits similar characteristics, with a significant clustering observed at the vortex position of the blade tip. As the distance along the axial direction increases, the clustering phenomenon begins to weaken. The sand particles clustered at the tip of the blade

gradually spread outward to about twice the rotor diameter and then begin to mix. This phenomenon is attributed to the wake deficit that the closer to the wind turbine region, the greater the wake velocity radial gradient. Such a velocity gradient formed the ring-shaped distribution and the diffusion of the sand cluster at the blade tip. In the region farther away from the wind turbine, the radial velocity gradient becomes smaller and the wake velocity increases to form the wake velocity recovery phenomenon, which leads to the weakening and disappearance of the clustering phenomenon. In the area where the wind turbine hub is located, there are also clustering phenomena observed at the blade root vortex, although in smaller numbers compared to the tip vortex. This discrepancy arises due to the omission of the wind turbine hub in the ALM. As a result, when the wind flows through the wind rotor, compression occurs at the center of the hub, leading to an increased velocity and a higher rate of sand particle passage. However, as the sand continues to develop and encounters resistance from the wake flow, sand particles gradually cluster, showing the clustering phenomenon at the
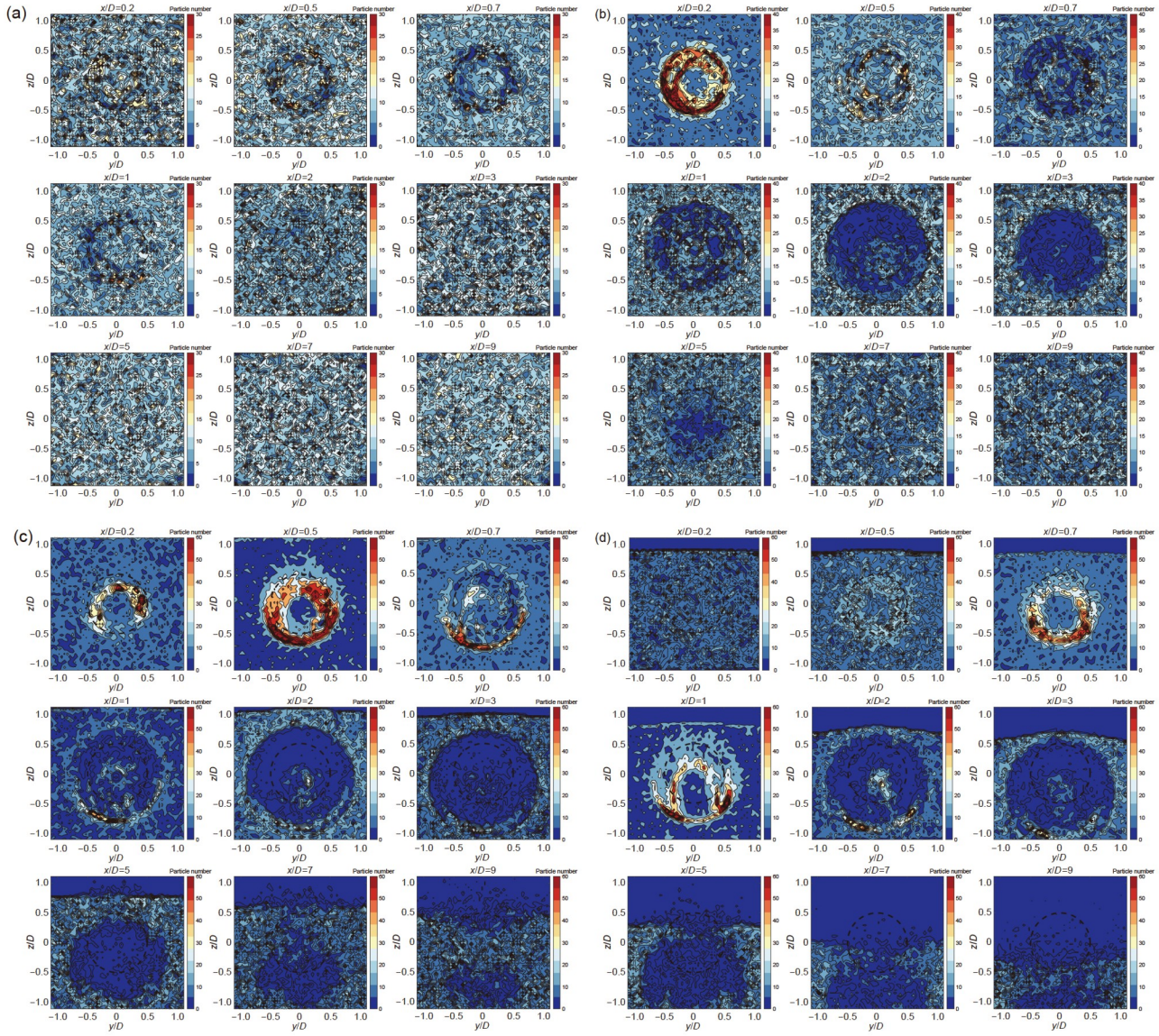
Figure 15 (Color online) Cloud maps of the distribution of the number of sand particles in different cross-sections during wind turbine operation. (a) Case B; (b) Case C; (c) Case D; (d) Case E.

center of 1*D*-3*D*. A comparison of cloud maps depicting the distribution of sand particles under varying particle size cases reveals that the degree of clustering among sand particles varies with different particle sizes. The concentration of sand particles exhibited a distinct "ring-shaped distribution", particularly at 0.2*D* and 0.5*D* in Case C and Case D. The phenomenon can be explained by the combined influence of centrifugal force and the tip vortex. As the particle size increases, the gravitational forces exert a greater influence on the particles, causing them to settle more easily and reducing their ability to remain suspended in the air for extended periods. As a result, there is an enhanced accumulation of particles at the lower blade tip compared to the upper blade tip, particularly evident in the 3*D* of Case D and Case

E. At the same time, the cross-section where the clustering phenomenon is most pronounced shifts backward with increasing particle size, influenced by the inertia of the particles. It is worth noting that Case B, which has a Stokes number much smaller than 1, exhibits stronger diffusivity, resulting in fewer particle clustering and faster intermixing.

To compare the obstruction effect of the wind turbine on sand particles of different particles sizes, the sand-blocking rate is defined as $I = (n_1 - n_2)/n_1$, where n_1 is the number of particles in the $-2D$ cross-section in front of the wind turbine and n_2 is the number of particles in different cross-section after the wind turbine. Positive values of I indicate a sand-blocking effect, while negative values suggest a clustering effect. The sand-blocking rate exhibits a clear regularity

characteristic, as evident in Figure 16(a). The negative value of *I* at the tip vortex indicates that the wind turbine induces particle clustering, with a more pronounced effect observed for larger particles. The positive value of *I* within the sweeping range of the wind turbine indicates that the wind turbine has a certain sand-blocking effect, which is also an obvious conclusion. Since the omission of the hub in the ALM, it results in a negative sand-blocking rate at the center of the hub.

To obtain the variation of sand-blocking rate with the development of wake, the data from different cross-section locations in Case C were collected and compared, as illustrated in Figure 16(b). As the wake distance increases, the average sand-blocking rate recorded for the four sections within the wind turbine swept surface shows the following variation: 27.83% at *x*/*D*=1, 67.55% at *x*/*D*=3, 41.40% at *x*/*D*=5, and 2.66% at *x*/*D*=7. The average sand-blocking rate showed an increasing and then decreasing trend with wake distance, peaking at *x*/*D*=3. This demonstrates the significant inhibitory effect of the wind turbine on sand transport, particularly in the near wake zone. The dimensionless sand-blocking rate provides a visual representation of the impact of the wind turbine on sand transport, by reflecting the change in sand concentration before and after the wind turbine.

4.3   Analysis of ground deposition of sand particles

Based on a consensus, it is widely acknowledged that the characteristics of the near-surface flow field exert a significant influence on the dry deposition of sand particles [41]. The wind turbine wake zone alters the atmospheric boundary layer flow characteristics, including changes in wind speed profiles due to wind speed deficit and changes in turbulence statistics due to various eddy structures. From an energy conservation perspective, wake turbulence results in

increased deposition due to the reduction of wind energy, which inevitably leads to a decrease in transport capacity. However, the turbulence effect is a combination of boundary layer shear turbulence and complex wake turbulence, and its impact on ground dry deposition for different particle sizes requires further investigation. For this reason, this paper temporarily omits the analysis of the near-surface dynamic behavior of sand particles and focuses on examining the distribution of ground dry deposition in the wake zone.

As shown in Figure 17, ground deposition in different wind-sand environments is based on the difference in the number of sand particles per unit area in the presence and absence of wind turbines $N_s = N_y - N_n$, with the gray cross-section denoting the plan where the wind turbines are located. The wake velocity deficit generated by the wind turbine reduces the sand transport rate, which leads to earlier ground deposition. Specifically, total ground deposition increased by 20.20%, 17.50%, 2.26%, and −1.64% in the case with the wind turbine compared to the case without the wind turbine, respectively. This phenomenon is due to the difference in particle size. Small-size particles are more susceptible to wake velocity deficit due to their lower inertia, leading to increased deposition. On the contrary, large particle size particles, despite being affected by the wake velocity deficit, have a stronger tendency to escape out of the computational domain under the influence of inertia, leading to less pronounced statistics of ground deposition than for small particle sizes. The statistics of ground deposition are even negative at particle sizes of 150 μm. In addition, we found that in the zone downstream of the wind turbine, significant deposition peaks and valleys occur for different particle sizes. It is worth noting that the rotational effect of the wind turbine wake and the centrifugal force on the sand particles result in a "triangular" distribution of deposition in the ground projection zone of the wake. These results indicate that the wake flow contributes significantly to particle
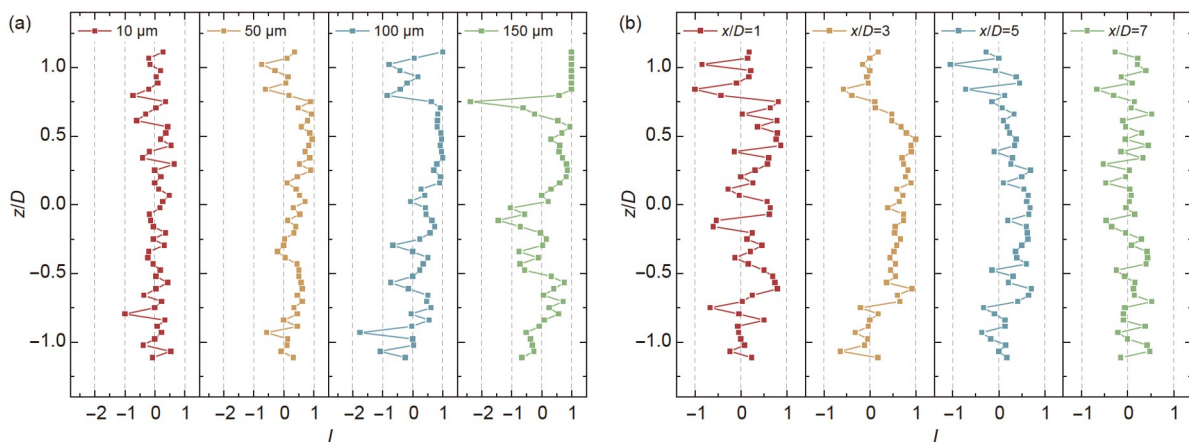

Figure 16   (Color online) Sand-blocking rate during wind turbine operation. (a) Sand-blocking rate at 2*D* cross-section for particles of different sizes; (b) Case C: Distribution of sand-blocking rate at different cross-sections in the wake zone.
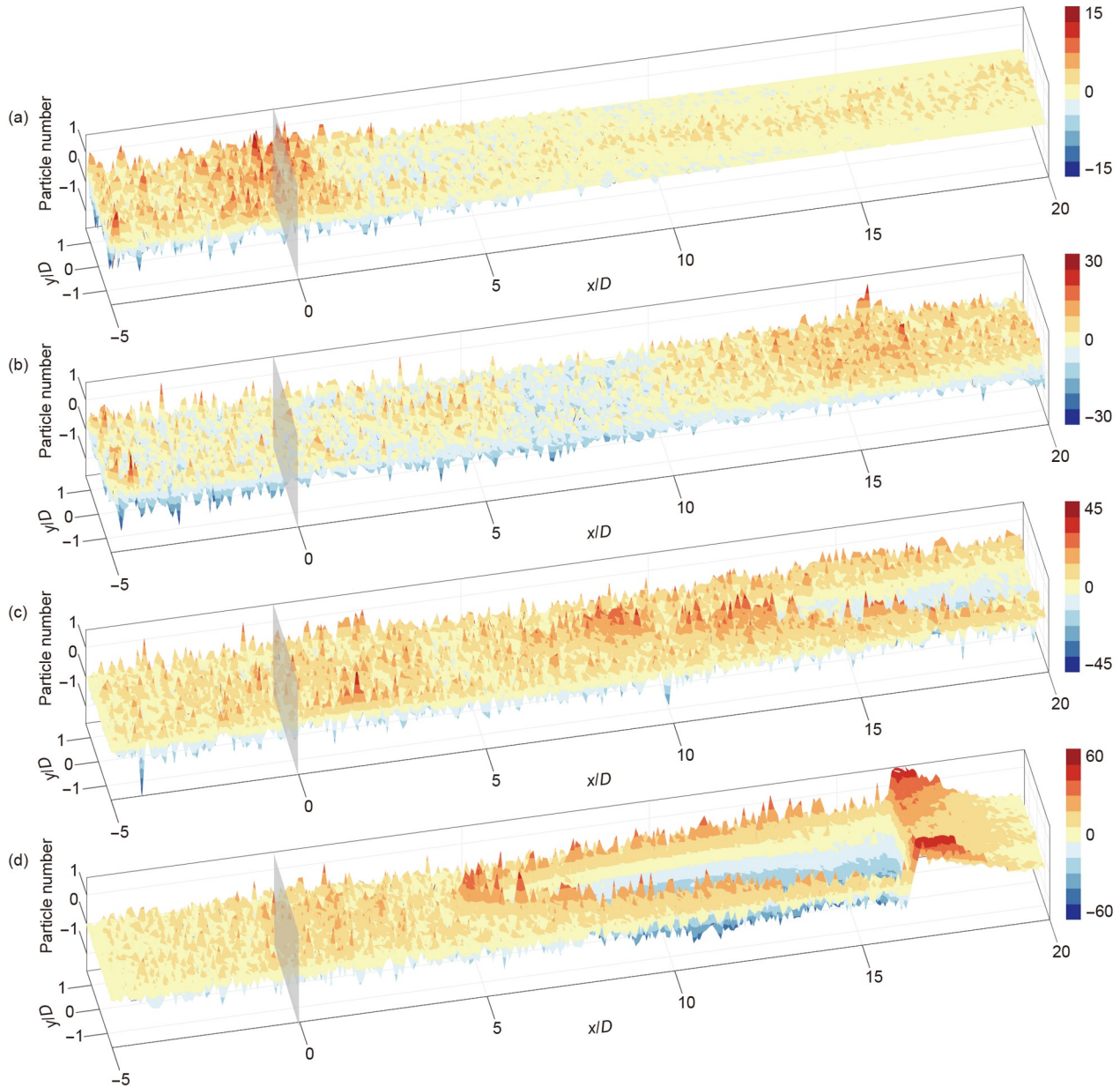
Figure 17 (Color online) Quantification of ground deposition in different wind-sand environments. (a) Case B; (b) Case C; (c) Case D; (d) Case E.

deposition. However, the rotational effect of the wake also leads to a change in the direction of particle velocity, which in turn affects the distribution of particle size and sand concentration within the corresponding ground zone of the wake, resulting in an inhomogeneous distribution. It also means that wind farms experiencing different levels of sandstorms or coming from various sand sources will exhibit varying variations in topsoil particles.

Figure 18 illustrates the variation in ground deposition as wake development progresses for different sand particle sizes. The dotted line represents ground deposition without the wind turbine, while the solid line shows ground deposition with the wind turbine. There is a clear overlap between the solid and dotted lines until $x/D = -2$, indicating that wind turbines have little effect on ground deposition in this zone. Following the wind turbines, there are distinct peaks and valleys in ground deposition, consistent with those depicted in Figure 17. In particular, in the absence of a wind turbine, the sand particles of 150 μm are strongly influenced by their gravity and have completely deposited at $x/D = 16$, resulting in a sudden drop of the ground deposition to 0. In the presence of a wind turbine, the wake effect of the wind turbine changes the trajectory of the sand particles, resulting in a longer transport distance.
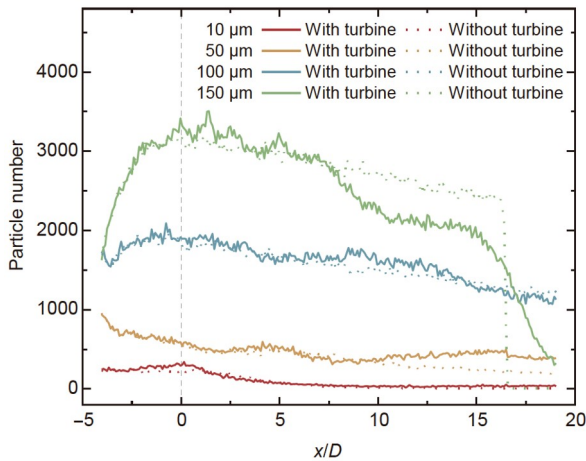
Figure 18　(Color online) Plotting ground deposition with wake development in different wind-sand environments.

5　Conclusions

In this study, we conducted a comprehensive analysis of the motion and distribution characteristics of sand particles with typical particle sizes in a wind turbine wake using a numerical method that combines ALM and LES within the open-source CFD software OpenFOAM. The research findings demonstrate that:

(1) Sand particles exhibit a spiral settling pattern after passing through the wind turbine, and they exhibit strong rotation characteristics in the near wake zone. This rotational effect weakens in the far wake zone, where particle velocity tends to stabilize. This process of wind turbine wake evolution is highly similar to that observed for sand particles.

(2) Sand particles tend to cluster in the peripheries of the vortex cores of low vorticity in the wake of the turbine, forming a distinctive "network structure". Small particles with low inertia respond rapidly to fluid motion and are uniformly distributed throughout the turbine wake. Instead, large particles with high inertia are less influenced by surrounding fluid motion, maintaining their motion characteristics and resisting suck by vortices. These large particles undergo significant settling under the influence of gravity.

(3) Tip vortices have a clustering effect on sand particles. As the transport distance increases, the particles that cluster at the tip of the blade spread outward to about twice the rotor diameter and begin to mix with the incoming environment. The wind turbine has a significant hindering effect on sand-dust transport. The average sand-blocking rate showed an increasing and then decreasing trend with the increase of wake distance, reaching 67.55% at the maximum.

(4) The wind turbine will induce early deposition of sand particles, with distinct deposition peaks and valleys downstream of the wind turbine. The total amount of ground deposition increased by 20.20%, 17.50%, 2.26%, and −1.64% for the four particle sizes with wind turbines compared to the case without wind turbines. Furthermore, the amount of deposition in the ground projection zone of the wind turbine wake shows a "triangular" distribution.

Our findings reveal the movement patterns and spatio-temporal distribution characteristics of sand particles within the wake of a wind turbine. The findings provide valuable insights into the design of wind turbines and the establishment of wind farms in arid regions. Nevertheless, it is imperative to acknowledge that the study has certain limitations. Firstly, we did not account for the influence of the hub on sand particle motion. Secondly, a comprehensive analysis of individual particle trajectories was not conducted, thus restricting our understanding of their specific behaviors. Future studies can further explore the impact mechanism of wind farm construction on the ecological environment in deserts, the Gobi, and other arid regions, and synthesize these deficiencies to obtain more comprehensive and accurate results. Furthermore, we expect to adapt this method to address the impact of salt or liquid droplets on offshore wind turbines [42], or sediment transport's impact on tidal current turbines [43], which are important concerns from those industry, and can be solved with similar numerical approach.

Conflict of interest　The authors declare that they have no conflict of interest.

1　Y. Wang, R. Wang, K. Tanaka, P. Ciais, J. Penuelas, Y. Balkanski, J. Sardans, D. Hauglustaine, W. Liu, X. Xing, J. Li, S. Xu, Y. Xiong, R. Yang, J. Cao, J. Chen, L. Wang, X. Tang, and R. Zhang, Nature **619**, 761 (2023).

2　M. G. Khalfallah, and A. M. Koliub, Desalination **209**, 209 (2007).

3　P. He, N. C. Chen, and D. M. Hu, Key Eng. Mater. **474-476**, 811 (2011).

4　D. Li, Z. Zhao, Y. Li, Q. Wang, R. Li, and Y. Li, Appl. Math. Mech.-Engl. Ed. **39**, 639 (2018).

5　Y. Li, F. Chen, R. Li, D. Li, and X. Guo, Int. Trans. Electr. Energ. Syst. **31**, e12541 (2021).

6　S. Baidya Roy, and J. J. Traiteur, Proc. Natl. Acad. Sci. USA **107**, 17899 (2010).

7　K. A. Adkins, and A. Sescu, Energies **15**, 2603 (2022).

8　J. Mo, T. Huang, X. Zhang, Y. Zhao, X. Liu, J. Li, H. Gao, and J. Ma, Atmos. Chem. Phys. **17**, 14239 (2017).

9　Q. Wang, K. Luo, C. Wu, and J. Fan, Energy **183**, 1136 (2019).

10　T. Wang, X. Zou, B. Li, Y. Yao, J. Li, H. Hui, W. Yu, and C. Wang, Mar. Pollut. Bull. **128**, 466 (2018).

11　Q. Dai, K. Luo, T. Jin, and J. Fan, J. Fluid Mech. **832**, 438 (2017).

12　G. Wang, H. Gu, and X. Zheng, Phys. Fluids **32**, 106604 (2020).

13　X. Zheng, G. Wang, and W. Zhu, J. Fluid Mech. **914**, A35 (2021).

14　A. Gunn, M. Wanker, N. Lancaster, D. A. Edmonds, R. C. Ewing, and D. J. Jerolmack, Geophys. Res. Lett. **48**, e2020GL090924 (2021).

15　Y. Shao, J. Zhang, M. Ishizuka, M. Mikami, J. Leys, and N. Huang, Atmos. Chem. Phys. **20**, 12939 (2020).

16　P. He, J. Zhang, H. J. Herrmann, and N. Huang, Sci. Bull. **67**, 1421

(2022).

17 K. Luo, J. Fan, W. Li, and K. Cen, Fuel **88**, 1294 (2009).

18 J. Yao, Y. Zhao, N. Li, Y. Zheng, G. Hu, J. Fan, and K. Cen, Ind. Eng. Chem. Res. **51**, 10936 (2012).

19 H. Homann, and J. Bec, Phys. Fluids **27**, 053301 (2015), arXiv: 1501.06755.

20 Z. Shi, F. Jiang, H. Strandenes, L. Zhao, and H. I. Andersson, Int. J. Multiphase Flow **130**, 103332 (2020).

21 Z. Shi, F. Jiang, L. Zhao, and H. I. Andersson, Int. J. Multiphase Flow **141**, 103678 (2021).

22 S. Lin, J. Liu, H. Xia, Z. Zhang, and X. Ao, Appl. Math. Model. **103**, 287 (2022).

23 S. E. Smith, K. N. Travis, H. Djeridi, M. Obligado, and R. B. Cal, Renew. Energy **164**, 346 (2021).

24 K. N. Travis, S. E. Smith, L. Vignal, H. Djeridi, M. Bourgoin, R. B. Cal, and M. Obligado, J. Fluid Mech. **933**, A42 (2022).

25 M. J. Andrews, and P. J. O'Rourke, Int. J. Multiphase Flow **22**, 379 (1996).

26 S. Elghobashi, Appl. Sci. Res. **52**, 309 (1994).

27 J. N. Sørensen, and W. Z. Shen, J. Fluids Eng. **124**, 393 (2002).

28 Z. Zheng, Z. T. Gao, D. S. Li, R. N. Li, Y. Li, Q. H. Hu, and W. R. Hu, Sci. China-Phys. Mech. Astron. **61**, 94712 (2018).

29 Z. Gao, Y. Li, T. Wang, W. Shen, X. Zheng, S. Pröbsting, D. Li, and R. Li, Renew. Energy **172**, 263 (2021).

30 Z. Gao, Y. Li, T. Wang, S. Ke, and D. Li, Appl. Math. Mech-Engl. **42**,

411 (2021).

31 C. R. Shapiro, D. F. Gayme, and C. Meneveau, J. Fluid Mech. **841**, R1 (2018).

32 M. Wang, H. Ming, W. Huo, H. Xu, J. Li, and X. Li, J. Arid Land **9**, 753 (2017).

33 H. Ming, M. Wei, and M. Wang, Atmosphere **10**, 511 (2019).

34 E. Liang, G. Ma, Y. Li, X. Zheng, F. Wu, S. Li, and D. Li, Sci. Sin-Phys. Mech. Astron. **53**, 234701 (2023).

35 G. Ma, J. Chang, D. Li, C. Huo, N. Liu, and R. Li, Acta Energ. Solaris Sin. **44**, 390 (2023).

36 G. Ma, C. Huo, D. Li, and J. Chang, Acta Energ. Solaris Sin. **44**, 444 (2023).

37 W. Zhang, C. D. Markfort, and F. Porté-Agel, Exp. Fluids **52**, 1219 (2011).

38 D. S. Li, T. Guo, Y. R. Li, J. S. Hu, Z. Zheng, Y. Li, Y. J. Di, W. R. Hu, and R. N. Li, Sci. China-Phys. Mech. Astron. **61**, 94711 (2018).

39 V. P. Stein, and H. J. Kaltenbach, J. Phys.-Conf. Ser. **753**, 032061 (2016).

40 R. Monchaux, M. Bourgoin, and A. Cartellier, Phys. Fluids **22**, 103304 (2010).

41 N. Huang, and J. Zhang, Proc. IUTAM **17**, 129 (2015).

42 X. Chen, Z. Jiang, Q. Li, Y. Li, and N. Ren, J. Offshore Mech. Arctic Eng. **142**, 052003 (2020).

43 Q. Hu, Y. Li, Y. Di, and J. Chen, J. Renew. Sustain. Energy **9**, 064501 (2017).